Short Article

Osteocytes regulate primary lymphoid organs and fat metabolism

Mari Sato[1,2], Noboru Asada[1], Yuko Kawano[1], Kanako Wakahashi[1], Kentaro Minagawa[1], Hiroki Kawano[1], Akiko Sada[1], Kyoji Ikeda[3], Toshimitsu Matsui[1], and Yoshio Katayama[1,4]

[1] Hematology, Department of Medicine, Kobe University Graduate School of Medicine, 7-5-1 Kusunoki-cho, Chuo-ku, Kobe 650-0017, Japan
[2] Biochemistry and Molecular Biology, Graduate School of Dental Medicine, Hokkaido University, North 13, West 7, Sapporo 060-8586, Japan
[3] Department of Bone and Joint Disease, National Center for Geriatrics and Gerontology (NCGG), 35 Gengo, Morioka, Obu, Aichi 474-8511, Japan
[4] PRESTO, Japan Science and Technology Agency, 4-1-8 Honcho, Kawaguchi, Saitama 332-0012, Japan

Running Title: Remote organ control by osteocytes

*Correspondence:
Yoshio Katayama, MD, PhD
Hematology, Department of Medicine,
Kobe University Graduate School of Medicine
7-5-1, Kusunoki-cho, Chuo-ku, Kobe 650-0017, Japan
Phone: +81-78-382-6912
Fax: +81-78-382-6910
e-mail: katayama@med.kobe-u.ac.jp

Summary

Osteocytes act as mechanosensors to control local bone volume. However, their roles in the homeostasis of remote organs are largely unknown. We show that ablation of osteocytes in mice (osteocyte-less (OL) mice) leads to severe lymphopenia due to lack of lymphoid-supporting stroma in both the bone marrow and thymus, and complete loss of white adipose tissues. These effects were reversed when osteocytes were replenished within the bone. In contrast, neither *in vivo* supply of T cell progenitors and humoral factors via shared circulation with a normal parabiotic partner, nor ablation of specific hypothalamic nuclei rescued thymic atrophy and fat loss in OL mice. Furthermore, ablation of the hypothalamus in OL mice led to hepatic steatosis, which was rescued by parabiosis with normal mice. Our results define a role for osteocytes as critical regulators of lymphopoiesis and fat metabolism, and suggest that bone acts as a central regulator of multiple organs.

Introduction

The bone is a sensory organ consisting of osteocytes and osteoblasts. Osteocytes comprise more than 90% of all bone cells and form a comprehensive network throughout skeletal tissues. Osteocytes contribute to bone homeostasis by converting mechanical stress to biological signals; hence the major players in bone turnover, osteoblasts and osteoclasts, are regulated locally on the bone surface (Bonewald, 2011; Klein-Nulend et al., 2013). Reduced mechanical stress to the bones of astronauts or bedridden patients leads to rapid progression of osteoporosis and impaired immunity (Belavy et al., 2011; Crucian and Sams, 2009; Gueguinou et al., 2009; Lang et al., 2004). However, it remains to be elucidated whether osteocytes are also critical for homeostasis of the immune system and even other organs. Here we address this issue, using a mouse model, in which targeted ablation of osteocytes induces osteoporosis with defective mechanotransduction (Tatsumi et al., 2007).

Results

Osteocyte ablation caused reversible lymphopenia and lymphoid organ atrophy

We first confirmed that local microgravity on the hind limbs during mouse tail suspension system, which is known to induce local bone loss (Globus et al., 1984), suppressed the osteocyte network formation in the bone and reduced the number of lymphocytes in the bone marrow (BM) of unloaded bone but not in the systemic circulation (Figures S1A-D). However, the hematopoietic phenotype in this system could not be due to the decreased stimulatory signals to osteocyte network by microgravity alone, but other factors could be responsible as well, e.g. less blood flow. To directly address the question if the osteocyte network is indispensable not only for the bone but also for other organs, we utilized transgenic (Tg) mouse model with targeted expression of diphtheria toxin receptor (DTR) under the promoter of dentin matrix protein-1 (DMP-1) (Tatsumi et al., 2007). Fifteen-week-old wild type (WT) and Tg littermate mice were injected with a single dose of diphtheria toxin (DT). The osteocyte-less (OL) mice showed a comparable lacunocanalicular interstitial fluid space with WT mice, and there was a marked reduction in neuron-like osteocyte network formed by projections at 3 weeks (Figures 1A, S1E, and S1F). Importantly, osteocytes seemed to be damaged in terms of reduced nuclear size, but they were not depleted in this experiment. The term “OL” in this study is

defined as the condition wherein some osteocytes are killed and ablated while others are tentatively compromised. The body weight declined steadily during the 3 weeks following DT injection (27.1 ± 2.0g and 20.8 ± 1.5g for WT and OL mice, respectively, n=10-11, $p<0.05$). Peripheral blood leukocyte count was significantly reduced in OL mice due to severe B and T lymphopenia (Figure 1B). A recent report has shown that the deletion of Gsα specifically in osteocytes strongly enhanced myelopoiesis due to the excess production of granulocyte colony-stimulating factor (G-CSF) presumably from osteocytes (Fulzele et al., 2013). However, OL mice showed no alteration in myelopoiesis, which implies that G-CSF from osteocytes during steady-state may not be indispensable. Drastic thymic atrophy with reduction of thymocytes by 90% was also found in OL mice (Figure 1C), as well as splenic atrophy (Figure 1D). These were not due to direct damage by DT in view of the specific expression of DMP-1/DTR in the bone (Figure S1G). The osteocytic network was restored at 100 days following DT administration in Tg mice (Figure 1E) presumably by embedding of intact osteoblasts then terminal differentiation to new osteocytes or from contribution of osteocytes which recovered from the damage. Consequently, lymphopenia and lymphoid organ atrophy were completely normalized (Figures 1F-H). These

results suggest a functional communication between the bone and lymphoid organs.

Impaired B lymphopoiesis in OL mice caused by depletion of lymphoid-specific stroma in bone marrow

We next evaluated lymphopoiesis in the BM, which is the primary organ for B-lymphogenesis. Although BM cellularity decreased only slightly, B220+/IgM-immature B cell fraction was markedly depleted in OL mice (Figures 2A and 2B). Hematopoietic stem cells (HSCs) were not affected in OL mice because the number of lineage-/IL-7Rα-/Sca-1+/c-kit+ cells was normal (Figure S2A). Furthermore, in the competitive repopulation assay, the chimerism of BM cells from OL mice was comparable to those from control mice (Figures S2B and S2C), which indicated that the lymphoid-specific defect in OL mice was ascribed to the hematopoietic microenvironment, but not to HSCs. While common lymphoid progenitors (CLP; lineage-/IL-7Rα+/Sca-1+/c-kit+) decreased only modestly, pro-B (B220+/IgM-/CD43+) and pre-B (B220+/IgM-/CD43-) cells were markedly reduced in numbers (Figures 2C-E). Results of colony-forming unit (CFU) assays were consistent with a lymphoid-specific defect; wherein, the

number of CFU-pre-B was greatly reduced in OL BM (Figure 2F), while myeloid CFU-granulocyte/macrophage (GM) was normal (Figure 2G). Thus, the marked decrease in B cells in the BM of OL mice took place at an early important step during B-lymphogenesis when the support by the specific stroma was required (Hardy et al., 1991). A key factor for B lymphopoiesis, CXCL12 (Egawa et al., 2001), was not decreased at neither the protein nor the mRNA level in OL mice BM (data not shown). Furthermore, to examine whether the impairment of B-lymphopoiesis was due to the decrease in osteocyte-secreted factors, we cultured WT BM cells on the layer of osteolineage cell lines, namely ST2 (mesenchymal stromal cells), MC3T3-E1 (osteoblastic cells), and MLO-Y4 (osteocytic cells). The results showed that B-lymphoid progenitor cells (B220+IgM- cells) were well maintained on the ST2 but not on the MC3T3-E1 and MLO-Y4 (Figure S2D). These data suggested that neither osteocyte-secreted molecules nor direct contact with osteocytes may be essential for the maintenance of B-lymphogenesis.

To investigate BM stromal cell function, we performed long-term BM cultures that specifically support B-lymphopoiesis (B-LTBMC) and myelopoiesis (M-LTBMC). Under B-LTBMC condition, BM cells from normal mice formed a

stromal layer and supported the production of small lymphoid-appearing B220+ cells. Strikingly, OL BM cultures did not produce small lymphoid-like cells but instead generated similar numbers of macrophages throughout the 6-week culture period (Figures 2H and 2I). In contrast, cultures from OL BM grown under M-LTBMC conditions were indistinguishable from those of normal mice (Figures S2E and S2F). The control adherent layer grown under B-LTBMC conditions contained approximately 30-40% of non-hematopoietic stromal cells (CD45-F4/80- and CD45-VCAM-1+), and the rest were macrophages (CD45+F4/80+). Noticeably, the vast majority of adherent cells in OL BM cultures were macrophages, and the non-hematopoietic stromal fraction was almost depleted (Figure 2J). Under M-LTBMC conditions, non-hematopoietic stromal cells were comparable between control and OL cultures (Figure S2G). Mesenchymal progenitors, as assessed by fibroblast colony-forming units (CFU-F) assay, were normal in OL BM (Figure 2K), and the switch from M- into B-LTBMC conditions gave rise to B cells together with normal stromal components (Figures S2H-J). These results suggested that the severe impairment of B-lymphopoiesis in OL BM was due to a depletion of B-lymphoid-specific stromal cells.

Osteocyte ablation caused thymocyte depletion due to defective microenvironment

The thymus, another primary lymphoid organ for T cells, was next investigated in OL mice. Owing to a marked reduction in cellularity of the thymus, the absolute cell numbers were reduced in all four CD4/CD8 fractions with a remarkable decrease in the percentage of the double positive fraction (Figure 3A). This finding seems to be caused by a specific deletion of osteocytes since targeted ablation of osteoblasts is not associated with alteration of the thymus (Visnjic et al., 2004). The absolute number of pro-T cells (CD3-/CD4-/CD8-/c-kit+/CD25-) in the thymus was greatly reduced (Figure 3B). Considering modest change only in CLP in the BM (Figure 2C), it would be reasonable to assume that the T cell progenitors supplied to the thymus could not proliferate because of environmental defect in OL thymus. Immunohistochemical staining of thymic epithelial cells (TEC) with keratin5 (K5) and keratin8 (K8) antibodies demonstrated that K8+ cortical epithelial area was drastically decreased, while K5+ medullary epithelial area was relatively preserved (Figure 3C). Likewise, K8+ cortical thymic epithelial meshwork

structure became sparse (Figure 3C), but that of K5+ medullary epithelium appeared normal (Figure S3A). Supply of T cell progenitors from OL BM into irradiated WT mice by bone marrow transplantation showed a normal reconstitution of thymocytes with normal distribution of K5+/K8+ epithelial cells (data not shown). Reciprocal transplantation was not assessed, since OL mice were too fragile as recipients. Moreover, the phenotype was transient for evaluation of T cell engraftment. Thus, we further examined OL thymic environment by using parabiotic model. The CD45.1-conjenic WT mice were surgically joined with CD45.2 WT or TG mice, and it was confirmed that the blood was equally shared (Figure S3B). After parabiotic pairs were maintained for 5-6 weeks after surgery, DT was injected to each mouse at age 15-week-old. Three weeks after osteocyte depletion, the thymus was evaluated. In CD45.1 WT and CD45.2 WT parabionts, a certain population of thymocytes showed normal differentiation in the parabiotic partners (Figure S3C). Importantly, the sharing of circulation with normal mice did not rescue thymic atrophy in OL mice (Figure 3D). Consistent with our hypothesis that the defect in T cell development was due to impaired microenvironment in the thymus, T cell progenitors derived from OL mice differentiated normally in the thymus of WT partner; whereas,

those from WT mice failed to differentiate in the thymus of OL partner (Figure 3E). These results indicate that in the absence of normal osteocyte network within the bone, microenvironment of the thymus is impaired, and the phenotype is not rescued by humoral factors from normal partners in the parabiotic experimental system.

Osteocytes regulated fat metabolism

In our study, the OL mice showed a progressive decrease in body weight in the course of few weeks after DT injection, and the weight gradually recovered along with the replenishment of osteocytes (Figure S4A). The OL mice lacked visible white adipose tissue (WAT) including subcutaneous, mesenteric, retroperitoneal fat tissue, and epididymal fat pad mass (Figure 4A). Plasma leptin level was decreased in association with fat loss (Figure S4B). This phenotype reminded us of human lipodystrophy (Garg, 2004; Huang-Doran et al., 2010; Simha and Garg, 2006); however, representative lipodystrophy-related genes were not affected in OL mice (Figure S4C). Despite a significant decrease in osteocalcin (Figure S4D), which has been reported to regulate insulin secretion in the pancreas and glucose metabolism (Ferron et al., 2010; Fulzele

et al., 2010), OL mice were not found to be diabetic (Figure S4E) in contrast to cases of human lipodystrophy. To examine whether lipid was consumed by the increased energy demand, energy expenditure was assessed during the period of body weight loss but it was rather decreased in OL mice (Figure S4F). These results suggest that lipid is not used, but is just lost after the ablation of osteocyte network. As there was a non-significant but slight trend of decrease in food intake (Figure S4G), we tested whether fat loss in OL mice could be rescued by high-fat diet. However, the results still showed the depletion of WAT and prevention of fatty liver (Figure S4H). Furthermore, it was unlikely that the fat/weight loss in OL mice was caused by digestive abnormalities since they had normal excrement with no signs of diarrhea or hematochezia. Endocrine malfunctions, such as hyperthyroidism and excess catecholamine secretion, were not possible causes also in view of the absence of increase in heart rate (not shown). In addition, the plasma concentration of corticosterone, which is secreted under a stressful condition and causes lipolysis or thymic atrophy, was not increased significantly in OL mice (Figure S4I). Because the sharing of circulation with normal mice by parabiosis did not rescue the fat loss induced by osteocyte depletion or cause any changes in the normal partner (data not

shown), fat/weight loss could not be attributed to the humoral mechanism. These results lead us to speculate that the integrity of osteocyte network is required for fat maintenance, and raise the possibility that osteocyte network within the bone controls fat metabolism through the central nervous system (CNS).

It is recognized that certain areas of the brain, such as the ventromedial hypothalamic nucleus (VMH) and arcuate nucleus (ARC), also control bone metabolism via the sympathetic nervous system in response to leptin signaling (Elefteriou et al., 2005; Takeda et al., 2002). Thus, we hypothesized that osteocytes might cooperate with the CNS to regulate fat metabolism. To test this, the VMH was ablated before osteocyte depletion. As expected, VMH ablation induced drastic obesity with high amount of WAT in both WT and Tg mice. After DT injection, thymic atrophy and peripheral WAT loss occurred in Tg mice irrespective of VMH ablation (Figures S4J and S4K). Strikingly, the liver of OL mice with ablated VMH became markedly enlarged and whitish in color due to severe fat accumulation (Figure 4B). This model of aberrant fat distribution recapitulates the phenotype of the human generalized lipodystrophy with hepatic steatosis (Garg, 2004). The sharing of circulation between VMH-ablated OL mice and normal partners by parabiosis, although the recovery of peripheral

WAT loss was not observed (data not shown), rescued the severe accumulation of fat in the liver (Figure 4C) suggestive of impaired fat clearance machinery in the liver. The expression of sterol regulatory element-binding protein-1c (SREBP1c) (Horton et al., 2002), a key lipogenic activator in non-alcoholic steatohepatitis (NASH), was markedly suppressed in VMH-ablated OL mice (Figure 4D) perhaps due to a negative feedback mechanism. The Fbxw7 (Onoyama et al., 2011), a ubiquitin ligase that promotes the degradation of SREBP1c, was not critically affected by VMH-ablation or osteocyte depletion. Importantly, the expression of microsomal triglyceride transfer protein (MTP), a main player in the fat clearance from the liver, and apoB (Letteron et al., 2003; Shindo et al., 2010) was increased by VMH-ablation most likely to dispose an increased fat intake, but the increase was cancelled by the depletion of osteocytes (Figure 4D). Ablation of ARC also induced obesity, and ARC-ablated OL mice exhibited fat loss and hepatic steatosis (data not shown). The expression of fat clearance genes in the liver, such as MTP and apoB, was suppressed by ARC-ablation (Figure 4D). Although each part of the brain may affect fat clearance from the liver through different mechanisms, a large amount of fat that flows out of peripheral WAT following osteocyte depletion may

accumulate in the liver, where the fat clearance system is impaired by the ablation of hypothalamic nuclei or osteocytic network. Levels of plasma free fatty acid (FFA) and triglyceride were severely decreased by osteocyte depletion; however, these levels were restored by the ablation of the VMH perhaps in association with fat accumulation in the liver (Figure S4L).

These data suggest that osteocytes may control fat maintenance in the whole body including the circulation, and the hypothalamus may cooperate with this system by regulating the liver function.

Bone environment after osteocyte depletion

This OL mouse model is known to not only induce osteocyte ablation, but also osteoclast activation (Tatsumi et al., 2007). One could think that rapid bone remodeling by the drastic activation of osteoclasts or inflammatory cytokines as triggered by damaged osteocytes might affect lymphopoiesis and fat metabolism. To address this concern, we examined the bone environment. As previously described (Tatsumi et al., 2007), the *RANKL* mRNA and the number of osteoclasts were slightly elevated in OL mice (Figures S4M and S4N). However, bone remodeling rate, as assessed by the calcein double labeling, did

not differ between WT and OL mice (Figure S4O). In addition, ovariectomy, known as a model of heightened bone remodeling, augments B lymphopoiesis and body weight according to the literature (Chen and Heiman, 2001; Erben et al., 1998; Wronski et al., 1986). Conversely, as a model of lowered bone remodeling, we assessed aged Tg mice (48-54 -week-old). After DT injection, similar phenotype as in 18-week-old mice was observed, including the drastic decrease of lymphoid progenitors and, to a lesser extent, fat loss (Figure S4P). Next, the level of inflammatory cytokines in the plasma and bone marrow extracellular fluid was measured, and there was no difference between WT and OL mice (Figures S4Q and S4R). Although the effect of osteocyte ablation on lymphopoiesis and fat metabolism could be partially influenced by the rate of bone remodeling or by the minor subpopulations of DMP-1-expressing cells in the thymic stroma or brain, these results suggested that majority of the phenotype in OL mice was a direct result of the lack of osteocyte function.

Discussion

This study reveals unexpected roles for bone osteocytes. The results suggest that bone governs lymphopoiesis through the regulation of the

microenvironment in primary lymphoid organs, and also controls fat metabolism throughout the body in cooperation with the brain (Figure 4E). Considering the reduced number of lymphocytes in the marrow of unloaded bone (Figures S1A-D), signals in the osteocyte network activated by gravity may be indispensable for the maintenance of multiple distant organs.

Although the signaling mechanism that links the bone with lymphoid organs or fat tissues remains to be elucidated, one potential candidate is the nervous system, given our previous observation of a rapidly progressive lymphopenia due to a lymphoid-specific stromal defect in UDP-galactose ceramide galactosyltransferase-deficient (*cgt*-/-) mice (Katayama and Frenette, 2003). The key enzyme for synthesis of major glycolipids in myelin sheath is cgt. The fact that *cgt*-/- mice display impaired neural conduction suggests that stromal-dependent lymphopoiesis is regulated by the nervous system. To examine whether osteocytes affect lymphopoiesis and fat metabolism through the nervous system, we performed chemical and surgical denervation such as adrenergic nerve destruction by 6-hydroxydopamine treatment, interception of the vagus nerve that innervates the thymus, or disruption of afferent nerves by capsaicin treatment before osteocyte depletion. However, none of these

interventions rescued the defect in OL mice (data not shown). In addition, nerve conduction velocity was normal in OL mice (data not shown). Further studies on humoral factors that cannot be supplied by parabiosis, as well as interaction of bone with the nervous system may be necessary.

Osteoblasts are now thought to be key players not only in bone homeostasis, but also in the maintenance of other organs (Karsenty and Ferron, 2012). Several genetic models of osteoblast-specific depletion by using osteocalcin promoter have been published to investigate the role of osteoblasts in vivo. However, osteocalcin promoter has high activity in differentiated osteoblasts but is also active in osteocytes which terminally differentiate from osteoblasts (O'Brien et al., 2004). In a model, inducible ablation of osteocalcin-expressing cells resulted in the alteration of both glucose and fat metabolisms (Yoshikawa et al., 2011). Interestingly, the administration of recombinant osteocalcin in this model reversed many of the abnormalities in glucose homeostasis but not the decreased fat in the gonad and liver. Together with our observations on OL mice, in which glucose metabolism does not appear to be altered but fat loss is prominent, osteoblasts and osteocytes may preferentially regulate glucose and fat metabolisms, respectively.

Our current findings imply that signals in the osteocyte network induced by the sensation of gravity are important for the maintenance of whole organ homeostasis and systemic health. Although the brain has been recognized as the central control of all organs, this study suggests that bone may also act as a central regulator of multiple organs.

Experimental Procedures

Mice

The DMP-1 DTR Tg mice (Tatsumi et al., 2007) were backcrossed for more than nine generations into C57BL/6 background before use. Fifteen-week-old WT and Tg littermate mice were injected with a single dose of DT (20 μ g/kg, i.p., Sigma-Aldrich Japan, Tokyo, Japan), and then samples were harvested and examined 3 weeks later (at 18-week-old) unless otherwise indicated. The C57BL/6-CD45.1 congenic mice were purchased from The Jackson Laboratory (BarHarbor, ME). All mice were fed a normal diet except the high fat diet experiment for Figure S4H. All animal experiments were approved by the Institutional Animal Care and Use Committee and were carried out according to the Kobe University Animal Experimentation Regulations.

Flow Cytometry

Antibodies: biotin mouse lineage panel, PE-anti-B220 (clone RA3-6B2), PE-anti-CD3ε (clone 145-2C11), PE-anti-c-kit (clone 2B8), FITC-anti-Sca-1 (clone E13-161.7), FITC-anti-CD45.2 (104), biotin-anti-CD45.1 (A20),

PE-anti-CD4 (GK1.5), FITC-anti-CD8 (53-6.7), and biotin-anti-CD25 (7D4) were from BD Pharmingen (San Diego, CA). FITC-anti-IgM was from Southern Biotech (Birmingham, AL). PE-Cy5-anti-IL-7R (A7R34), APC-anti-CD45.2 (104), biotin-anti-F4/80 (BM8), biotin-anti-VCAM-1 (429), APC-streptavidin, and PE-streptavidin were from eBioscience (San Diego, CA). Cells were suspended in PBS/0.5% BSA/2mM EDTA. Adherent cells in long-term BM cultures were stained after trypsinization and were analyzed using high-side scatter gating as previously described (Katayama and Frenette, 2003). Cell analyses were performed on a FACSCalibur flow cytometer with CellQuest software (Becton Dickinson, Mountain View, CA) and MoFlo^{TM} XDP flow cytometer with summit software (Beckman Coulter, Harbor Blvd, CA).

Cell Isolation and CFU Assays

Bone marrow cells were harvested by flushing the femora aseptically in RPMI, and single-cell suspension was obtained by gentle aspiration several times. The suspension volume was measured with a graduated pipette. The CFU-GM assays were done by inoculating bone marrow mononuclear cells into Methocult

M3534 media (StemCell Technologies, Vancouver, Canada) according to manufacturer's recommendation. The IL-7-dependent CFU-pre-B assays were done using Methocult M3630, and CFU-F cells were assayed in MesenCult Basal Medium supplemented with Mesenchymal Stem Cell Stimulatory Supplement (StemCell Technologies).

Co-cultures of bone marrow cells with osteolineage cell lines

ST2 (mesenchymal stromal cells), MC3T3-E1 (osteoblastic cells), and MLO-Y4 (osteocytic cells) were grown to semi-confluence in αMEM supplemented with 10% fetal bovine serum (FBS) in six-well culture plates. The medium was removed, and $1x10^6$ adherent cell-depleted bone marrow samples from 7-week old WT mice were cultured with or without the osteolineage cell layer in RPMI1640 supplemented with 5% FBS and $5x10^{-5}$ M 2-mercaptoethanol at 37℃ for 4 days. Floating cells were analyzed for B220/IgM expression by flow cytometry.

Long-Term Bone Marrow Cultures

The B- and M-LTBMC were performed exactly as previously described (Katayama and Frenette, 2003).

Generation of chimeric mice

Chimeric mice were generated by injection of 5 x 10^6 WT or OL mice (CD45.2) bone marrow nucleated cells (BMNCs) into lethally-irradiated (14 Gy, split dose) CD45.1 mice. Reconstitution by donor cells was confirmed in all mice by blood cell count and CD45.1/CD45.2 chimerism of peripheral blood leukocytes monthly. For competitive reconstitution, 1 x 10^6 BMNCs from DT-injected WT or OL mice (CD45.2) were injected together with 1 x 10^6 fresh BM competitor cells (CD45.1) into lethally-irradiated (14Gy, split dose) C57BL/6-CD45.1 congenic mice. Blood was harvested monthly from recipient mice, and the expressions of CD45.1 and CD45.2 were assessed by flow cytometry.

Parabiosis

Pairs of 9-10-week-old mice were anaesthetized and prepared for surgery. Mirror image incisions at the left and right flanks, respectively, were made through the skin. The skin of the adjacent parabiont was sutured together. Cross-circulation was determined in a subset of parabiotic pairs by measuring the frequency of blood cells from one partner (CD45.1) in the blood of the other partner (CD45.2). Each mouse, including WT partner, was injected with DT 5-6 weeks after the surgery (at 15-week-old) and then euthanized 3 weeks after DT injection. Blood chimerism at the time of euthanization was typically between 40% and 60%.

Histological analysis

Liver tissue was frozen in OCT compound (Sakura Fine Technical, Tokyo, Japan) and stained with H&E and Oil red O according to standard procedures. Femoral bones were fixed overnight in 4% paraformaldehyde (PFA), frozen in OCT compound, sectioned and stained for TRAP with TRAP/ALP Stain Kit (Wako, Tokyo, Japan). Histological staining to visualize bone interstitial fluid space using FITC was performed as described (Ciani et al., 2009). Bone labeling with peritoneal injection of calcein (20mg/kg body weight; Dojinwako, Tokyo,

Japan) was performed at 5 and 2 days before death in mice used for histomorphometry. The fluorescent signal derived from calcein labeling was analyzed using LSM510 confocal laser scanning (CLS) microscopy system (Carl Zeiss, Oberkochen, Germany).

Immunofluorescence Microscopy

Femoral bones were decalcified in 10% EDTA (pH 7.4) for 2 weeks, snap-frozen in liquid nitrogen-chilled hexane, and sectioned at 10μm thickness. Sections were fixed with 4% PFA for 10min, stained with anti-CD44 (BD Pharmingen) followed by donkey Alexa-488-anti-rat IgG (Invitrogen, Carlsbad, CA), and mounted in Vectashield Mounting Medium with 4,6-diamidino-2-phenylindole (DAPI) (Vector Laboratories, Burlingame, CA). For phalloidin staining, the sections were stained with Alexa488-conjugated phalloidin (Life Technologies Japan, Tokyo, Japan) and mounted with Vectashield Mounting Medium with DAPI. Images were captured using LSM510 CLS microscopy system (Carl Zeiss). Thymic cryosections (5μm) were fixed with 4% PFA and stained with anti-mouse keratin 5 (Troma-1; Developmental Studies Hybridoma Bank,

University of Iowa, Iowa City, IA) and anti–keratin 8 (Covance Research Products, Berkeley, CA). Goat Alexa-488-anti-rat IgG and goat Alexa-555-anti-rabbit IgG (Invitrogen) were used as secondary antibodies. Images were captured using KEYENCE BZ-9000 fluorescent microscope (Keyence, Osaka, Japan).

RNA Extraction and Q-PCR

Total RNA was extracted from BMNCs using TRIzol solution (Invitrogen). The bone carcass and other tissues were then immersed in liquid nitrogen, and pulverized into powder followed by RNA extraction with TRIzol. Total RNA (2μg) was treated with DNaseI (Invitrogen), and reverse transcribed using first strand cDNA synthesis with random primers (Promega, Madison, WI). The Q-PCR was performed using SYBRGreen (Life Technologies Japan) on LightCycler® 480 System (Roche Diagnostics, Mannheim, Germany). Primers used are listed in Table S1. All experiments were done in triplicate and normalized to *β-actin*.

Pharmacological disruption of neurons or CNS

Ablation of VMH and ARC was done as described elsewhere (Takeda et al., 2002). Briefly, to ablate VMH, four-week-old mice were given a single intraperitoneal injection with Gold thioglucose (GTG) (0.5 mg/g of body weight, Research Diagnostics, Inc., NJ). To ablate ARC, 2-day-old C57BL/6 pups were given daily subcutaneous injections of monosodium glutamate (MSG) (2 mg/g, Sigma-Aldrich Japan) for 9 days. DT was injected at the age of 15-week-old.

Metabolic studies

The energy expenditure measurements were obtained using an 8-chamber Oxymax system (Columbus Instruments, Columbus, OH). After 5 days acclimation to the apparatus, data for 24hr measurement were exported to Comma Separated Value (CSV) files and analyzed as recommended by manufacturer.

Plasma leptin, plasma insulin, and osteocalcin concentrations in the plasma and bone marrow extracellular fluid (BMEF; obtained as previously described (Katayama et al., 2006)) were measured with ELISA kits (BioVendor Candler, NC; Shibayagi, Gunma, Japan; Biomedical Technologies Inc., Stoughton, MA,

respectively). Plasma corticosterone levels were determined by liquid chromatography-tandem mass spectrometry (LC-MS/MS). Plasma FFA and triglyceride concentrations were measured with NEFA C test and Triglyceride E test (Wako), respectively. Blood glucose levels were determined by glucose oxidase method using Glutest Sensor Neo (Sanwa Kagaku, Kyoto, Japan).

Measurement of inflammatory cytokines

The levels of cytokines (TNF-α, IL-12p70, IL-6, IFN-γ, IL-10, MCP-1, and IL-1 beta) in the plasma and BMEF from WT and OL mice were quantitated using a mouse inflammation cytometric bead array (CBA) kit (BD Biosciences) and mouse IL-1 beta FlowCytomix (eBioscience), according to the manufacturer's instructions. Data were acquired with a FACSCan flow cytometer (Becton Dickinson) and analyzed with BD CBA Software (BD Biosciences).

Statistical Analysis

All values were given as mean ± SEM. Comparisons between groups were made by Student's *t*-test.

Supplemental Information

Supplemental information includes four supplemental figures and one supplemental table, and can be found with this article online.

Acknowledgments

We thank Prof. Lynda Bonewald (University of Missouri- Kansas City) for providing MLO-Y4 cells; Drs. T. Suzuki and S. Ishii for their help with mouse maintenance; Ms. C. Fukui for her technical assistance. This work was supported by the Grants-in-Aid for Young Scientist Start-up (#21890142 to M. Sato), Research Fellowships for Young Scientists (#22-481 to M. Sato), and Scientific Research (#23390251 to Y. Katayama) from Japan Society for the Promotion of Science; and the Grants-in-Aid for Scientific Research on Innovative Areas from the Ministry of Education, Culture, Sports, Science and

Technology in Japan (#23118517 to Y. Katayama), and also by Mochida Memorial Foundation and Takeda Science Foundation (to Y. Katayama).

Conflict-of-interest disclosure: The authors declare no competing financial interests.

References

Belavy, D.L., Beller, G., Armbrecht, G., Perschel, F.H., Fitzner, R., Bock, O., Borst, H., Degner, C., Gast, U., and Felsenberg, D. (2011). Evidence for an additional effect of whole-body vibration above resistive exercise alone in preventing bone loss during prolonged bed rest. Osteoporosis international : a journal established as result of cooperation between the European Foundation for Osteoporosis and the National Osteoporosis Foundation of the USA *22*, 1581-1591.

Bonewald, L.F. (2011). The amazing osteocyte. Journal of bone and mineral research : the official journal of the American Society for Bone and Mineral Research *26*, 229-238.

Chen, Y., and Heiman, M.L. (2001). Increased weight gain after ovariectomy is not a consequence of leptin resistance. American journal of physiology Endocrinology and metabolism *280*, E315-322.

Ciani, C., Doty, S.B., and Fritton, S.P. (2009). An effective histological staining process to visualize bone interstitial fluid space using confocal microscopy. Bone *44*, 1015-1017.

Crucian, B., and Sams, C. (2009). Immune system dysregulation during spaceflight: clinical risk for exploration-class missions. Journal of leukocyte biology *86*, 1017-1018.

Egawa, T., Kawabata, K., Kawamoto, H., Amada, K., Okamoto, R., Fujii, N., Kishimoto, T., Katsura, Y., and Nagasawa, T. (2001). The earliest stages of B cell development require a chemokine stromal cell-derived factor/pre-B cell growth-stimulating factor. Immunity *15*, 323-334.

Elefteriou, F., Ahn, J.D., Takeda, S., Starbuck, M., Yang, X., Liu, X., Kondo, H., Richards, W.G., Bannon, T.W., Noda, M.*, et al.* (2005). Leptin regulation of bone resorption by the sympathetic nervous system and CART. Nature *434*, 514-520.

Erben, R.G., Raith, S., Eberle, J., and Stangassinger, M. (1998). Ovariectomy augments B lymphopoiesis and generation of monocyte-macrophage precursors in rat bone marrow. The American journal of physiology *274*, E476-483.

Ferron, M., Wei, J., Yoshizawa, T., Del Fattore, A., DePinho, R.A., Teti, A., Ducy, P., and Karsenty, G. (2010). Insulin signaling in osteoblasts integrates bone remodeling and energy metabolism. Cell *142*, 296-308.

Fulzele, K., Krause, D.S., Panaroni, C., Saini, V., Barry, K.J., Liu, X., Lotinun, S., Baron, R., Bonewald, L., Feng, J.Q., *et al.* (2013). Myelopoiesis is regulated by osteocytes through Gsalpha-dependent signaling. Blood *121*, 930-939.

Fulzele, K., Riddle, R.C., DiGirolamo, D.J., Cao, X., Wan, C., Chen, D., Faugere, M.C., Aja, S., Hussain, M.A., Bruning, J.C., *et al.* (2010). Insulin receptor signaling in osteoblasts regulates postnatal bone acquisition and body composition. Cell *142*, 309-319.

Garg, A. (2004). Acquired and inherited lipodystrophies. The New England journal of medicine *350*, 1220-1234.

Globus, R.K., Bikle, D.D., and Morey-Holton, E. (1984). Effects of simulated weightlessness on bone mineral metabolism. Endocrinology *114*, 2264-2270.

Gueguinou, N., Huin-Schohn, C., Bascove, M., Bueb, J.L., Tschirhart, E., Legrand-Frossi, C., and Frippiat, J.P. (2009). Could spaceflight-associated immune system weakening preclude the expansion of human presence beyond Earth's orbit? Journal of leukocyte biology *86*, 1027-1038.

Hardy, R.R., Carmack, C.E., Shinton, S.A., Kemp, J.D., and Hayakawa, K. (1991). Resolution and characterization of pro-B and pre-pro-B cell stages in normal mouse bone marrow. The Journal of experimental medicine *173*, 1213-1225.

Horton, J.D., Goldstein, J.L., and Brown, M.S. (2002). SREBPs: activators of the complete program of cholesterol and fatty acid synthesis in the liver. The Journal of clinical investigation *109*, 1125-1131.

Huang-Doran, I., Sleigh, A., Rochford, J.J., O'Rahilly, S., and Savage, D.B. (2010). Lipodystrophy: metabolic insights from a rare disorder. The Journal of endocrinology *207*, 245-255.

Karsenty, G., and Ferron, M. (2012). The contribution of bone to whole-organism physiology. Nature *481*, 314-320.

Katayama, Y., Battista, M., Kao, W.M., Hidalgo, A., Peired, A.J., Thomas, S.A., and Frenette, P.S. (2006). Signals from the sympathetic nervous system regulate hematopoietic stem cell egress from bone marrow. Cell *124*, 407-421.

Katayama, Y., and Frenette, P.S. (2003). Galactocerebrosides are required postnatally for stromal-dependent bone marrow lymphopoiesis. Immunity *18*, 789-800.

Klein-Nulend, J., Bakker, A.D., Bacabac, R.G., Vatsa, A., and Weinbaum, S. (2013). Mechanosensation and transduction in osteocytes. Bone *54*, 182-190.

Lang, T., LeBlanc, A., Evans, H., Lu, Y., Genant, H., and Yu, A. (2004). Cortical and trabecular bone mineral loss from the spine and hip in long-duration spaceflight. Journal of bone and mineral research : the official journal of the American Society for Bone and Mineral Research *19*, 1006-1012.

Letteron, P., Sutton, A., Mansouri, A., Fromenty, B., and Pessayre, D. (2003). Inhibition of microsomal triglyceride transfer protein: another mechanism for drug-induced steatosis in mice. Hepatology *38*, 133-140.

O'Brien, C.A., Jia, D., Plotkin, L.I., Bellido, T., Powers, C.C., Stewart, S.A., Manolagas, S.C., and Weinstein, R.S. (2004). Glucocorticoids act directly on osteoblasts and osteocytes to induce their apoptosis and reduce bone formation and strength. Endocrinology *145*, 1835-1841.

Onoyama, I., Suzuki, A., Matsumoto, A., Tomita, K., Katagiri, H., Oike, Y., Nakayama, K., and Nakayama, K.I. (2011). Fbxw7 regulates lipid metabolism and cell fate decisions in the mouse liver. The Journal of clinical investigation *121*, 342-354.

Shindo, N., Fujisawa, T., Sugimoto, K., Nojima, K., Oze-Fukai, A., Yoshikawa, Y., Wang, X., Yasuda, O., Ikegami, H., and Rakugi, H. (2010). Involvement of microsomal triglyceride transfer protein in nonalcoholic steatohepatitis in novel spontaneous mouse model. Journal of hepatology *52*, 903-912.

Simha, V., and Garg, A. (2006). Lipodystrophy: lessons in lipid and energy metabolism. Current opinion in lipidology *17*, 162-169.

Takeda, S., Elefteriou, F., Levasseur, R., Liu, X., Zhao, L., Parker, K.L., Armstrong, D., Ducy, P., and Karsenty, G. (2002). Leptin regulates bone formation via the sympathetic nervous system. Cell *111*, 305-317.

Tatsumi, S., Ishii, K., Amizuka, N., Li, M., Kobayashi, T., Kohno, K., Ito, M., Takeshita, S., and Ikeda, K. (2007). Targeted ablation of osteocytes induces osteoporosis with defective mechanotransduction. Cell metabolism *5*, 464-475.

Visnjic, D., Kalajzic, Z., Rowe, D.W., Katavic, V., Lorenzo, J., and Aguila, H.L. (2004). Hematopoiesis is severely altered in mice with an induced osteoblast deficiency. Blood *103*, 3258-3264.

Wronski, T.J., Walsh, C.C., and Ignaszewski, L.A. (1986). Histologic evidence for osteopenia and increased bone turnover in ovariectomized rats. Bone *7*, 119-123.

Yoshikawa, Y., Kode, A., Xu, L., Mosialou, I., Silva, B.C., Ferron, M., Clemens, T.L., Economides, A.N., and Kousteni, S. (2011). Genetic evidence points to an osteocalcin-independent influence of osteoblasts on energy metabolism. Journal of bone and mineral research : the official journal of the American Society for Bone and Mineral Research *26*, 2012-2025.

Figure Legends

Figure 1. Osteocyte ablation causes reversible lymphopenia and lymphoid organ atrophy

(A) Immunofluorescence staining of femoral cortical bone of WT (left) and OL (right) mice. Images of CD44 and DAPI staining were merged. Original magnification x100. (B) Peripheral blood cells were analyzed for surface expression of B and T lymphocyte or myeloid markers (n=6-7).

(C, D) Gross appearance (top panels) and hematoxilin and eosin (H&E)-stained sections (middle panels, original magnification x4), and organ cellularity (bottom panels, n=7-9) of WT or OL thymus (C) and spleen (D).

(E-H) Representative femoral sections of WT or OL mice at 100 days following DT administration that showed recovery of osteocyte network formation along with osteocyte regeneration (E, original magnification x100). Peripheral blood cell counts (F), thymus (G) and spleen (H) cellularity were also restored (n=4). Data in B-D, F-H are shown as mean values ± SEM. *p<0.05, **p<0.01, ***p<0.001. See also Figure S1.

Figure 2. Impaired B lymphopoiesis in OL mice due to depletion of lymphoid-specific stroma in bone marrow

(A) WT versus OL mice BM cellularity (n=8-9).

(B-E) BM nucleated cells were analyzed for surface expression of CLP (C, n=10) or markers of different stages of B lymphocyte progenitors (B, D, and E, n=3-4).

(F, G) Frequency of CFU-pre-B (n=5) and CFU-GM (n=7-8).

(H) In B-LTBMC, OL mice BM produced larger floating cells than those from WT BM. Original magnification x 40. The inset shows May-Giemsa-stained cytospin preparations.

(I) Percentages of B220+ cells among floating cells in B-LTBMC at the indicated periods after initiation of cultures (n=3-4).

(J) FACS analysis of adherent cells in B-LTBMC. Red-gated CD45-stromal cells were greatly reduced in OL mice B-LTBMC (n=4).

(K) The number of CFU-fibroblast (CFU-F) in WT and OL mice BM (n=3).

Data in A, C-G, I, and K are shown as mean values ± SEM. *$p<0.05$, **$p<0.01$.

See also Figure S2.

Figure 3. Osteocyte ablation causes thymocyte depletion due to defective microenviroment

(A) FACS analysis of surface expression of T cell markers in WT versus OL mice thymus (n=6).

(B) Number of pro-T cells in the thymus (n=6).

(C) Immunofluorescent staining of K5 (red), K8 (green), and DAPI (blue) in the thymus. Upper panel, original magnification x4. Lower panel, cortical thymic epithelial cells (CTEC) stained with K8 were merged with DAPI. Magnifications x100.

(D, E) Experimental design of parabiosis. A CD45.2 WT or Tg mouse was joined with a CD45.1 WT mouse and maintained for 5-6 weeks (E, n=7). At 3 weeks following DT injection, thymic cellularity was quantified (D). Nucleated cells were isolated from the thymus of DT-injected CD45.1 WT and CD45.2 Tg (OL) parabiotic pairs and analyzed for T cell marker by FACS (E). Representative red plots of thymocytes originated from a CD45.2 OL mouse, and blue plots originated from a CD45.1 WT mouse (n=7).

Data in B, D are shown as mean values ± SEM. **p<0.01, ***p<0.001. See also Figure S3.

Figure 4. Osteocytes regulate fat metabolism

(A) Gross appearance of subcutaneous, mesenteric, and epididymal fat tissues of WT and OL mice. Epididymal fat pad weight to body weight ratio in WT and OL mice (n=3). n.d.: not detectable.

(B) Gross appearance, H&E stained sections and oil red O stained sections of the liver from the indicated mice (original magnification x10).

(C) Gross appearance, H&E stained sections and oil red O stained secstions of the liver of indicated parabiotic pairs (original magnification x10).

(D) Real-time PCR analysis of *SREBP1c, Fbxw7*, *MTP*, and *apoB* mRNA in the livers of the indicated mice. Expression levels were normalized for *β-actin* (n=4-5).

(E) Schematic illustration of “Bone as a central regulator of multiple organs”.

Data in A and D are shown as mean values ± SEM. *p<0.05, **p<0.01, ***p<0.001. See also Figure S4.

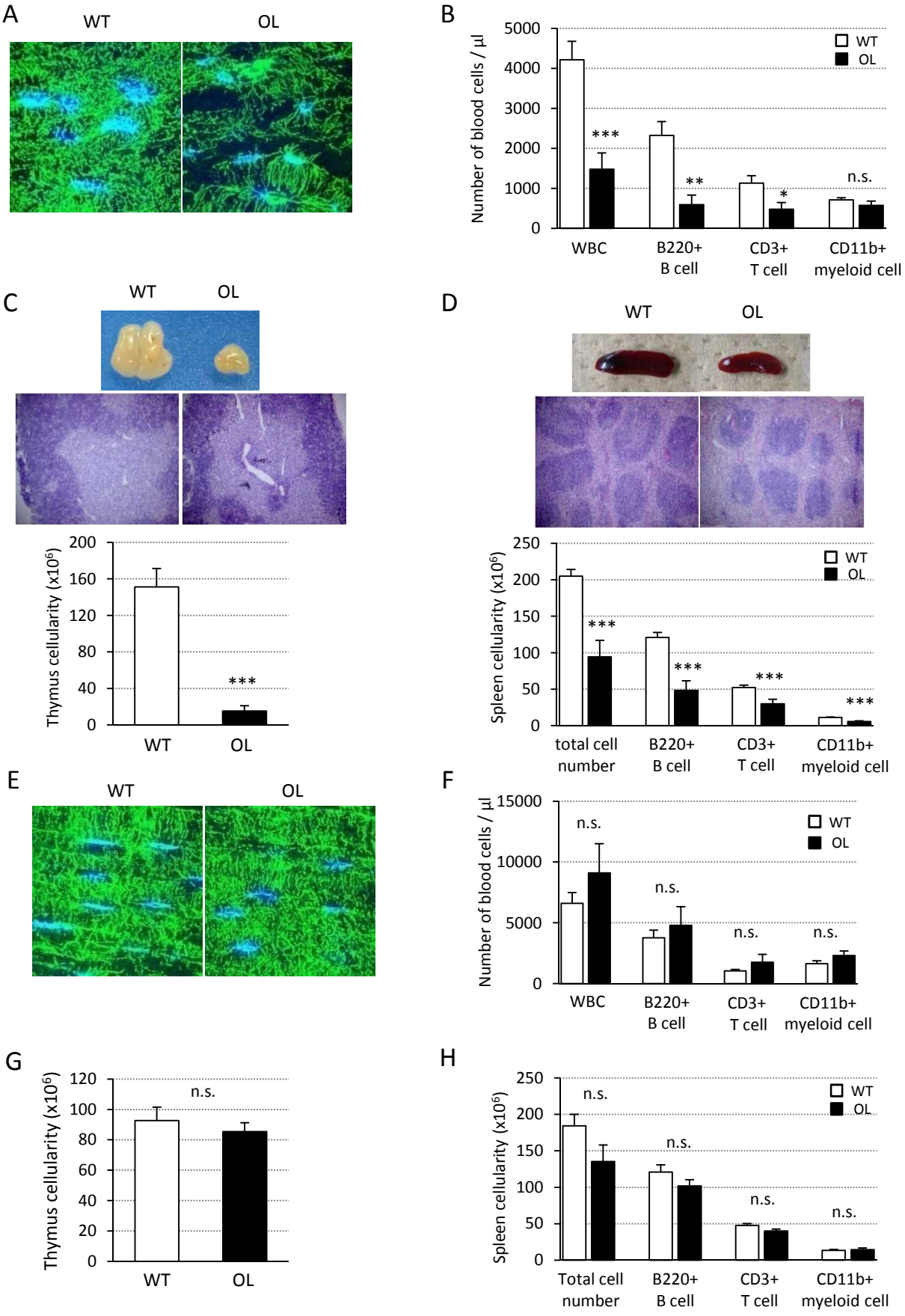

Figure 1 | Osteocyte ablation causes reversible lymphopenia and lymphoid organ atrophy.

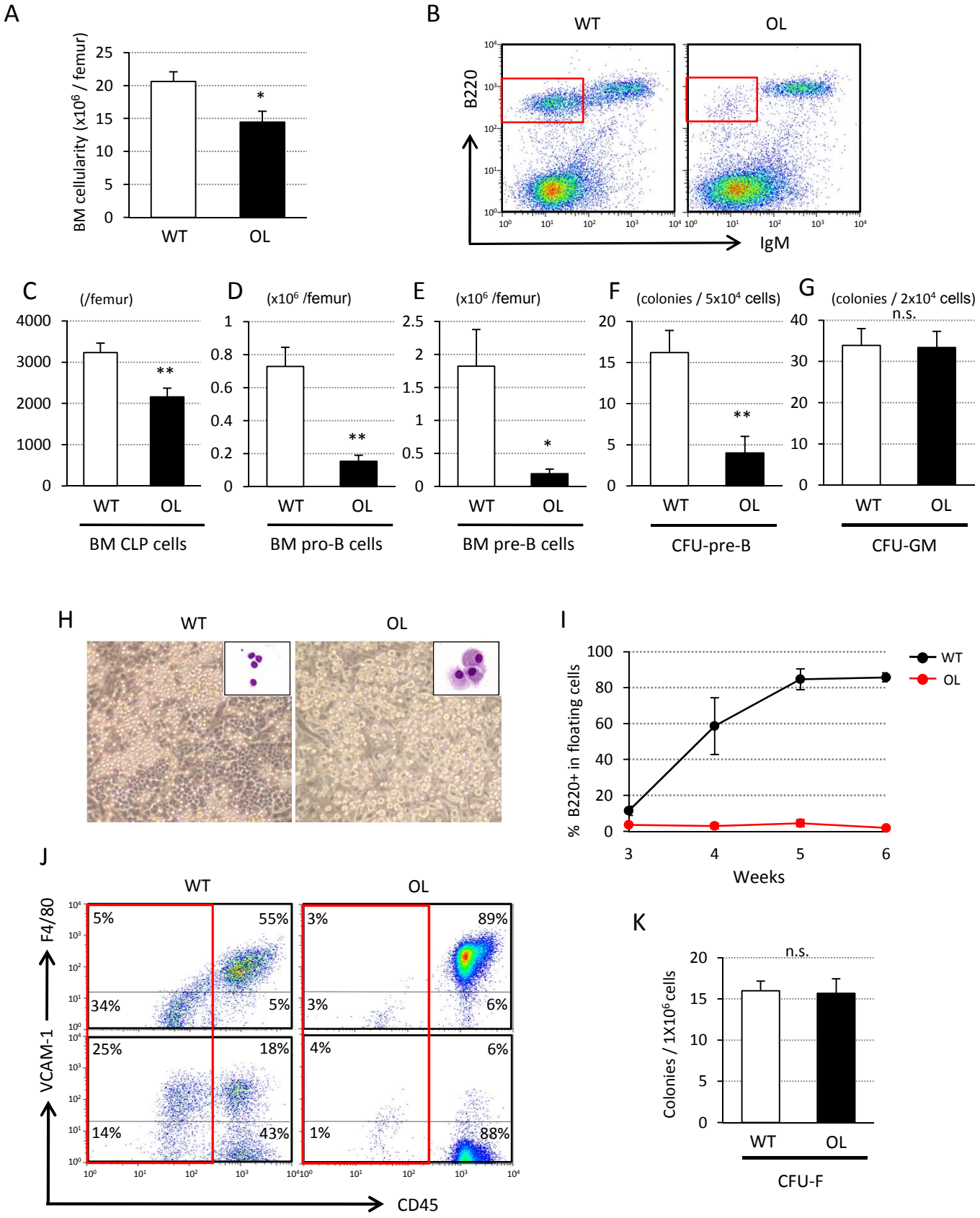

Figure 2 | Impaired B lymphopoiesis in OL mice due to depletion of lymphoid specific stroma in bone marrow.

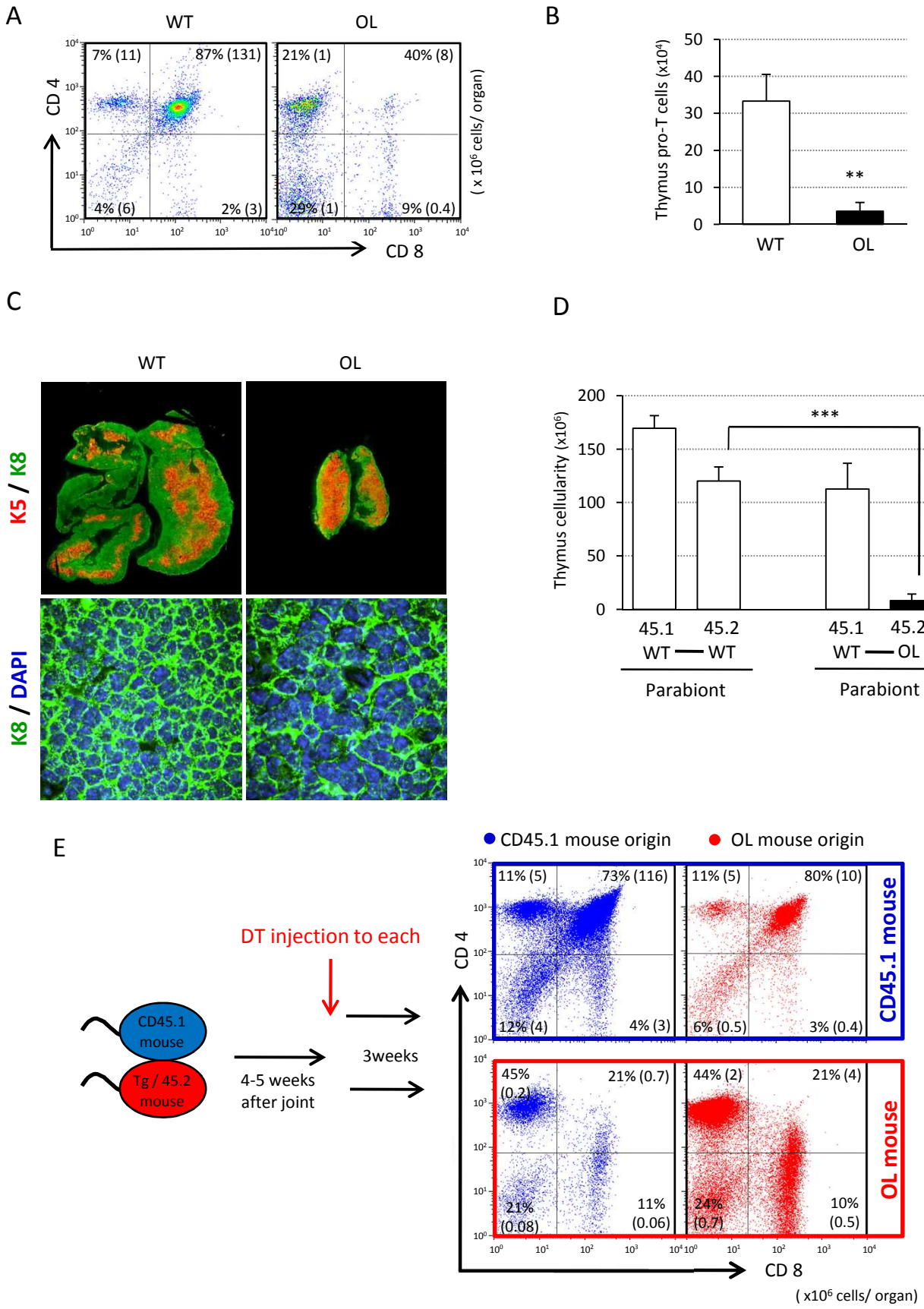

Figure 3 | Osteocyte ablation causes thymocyte depletion due to defective microenviroment.

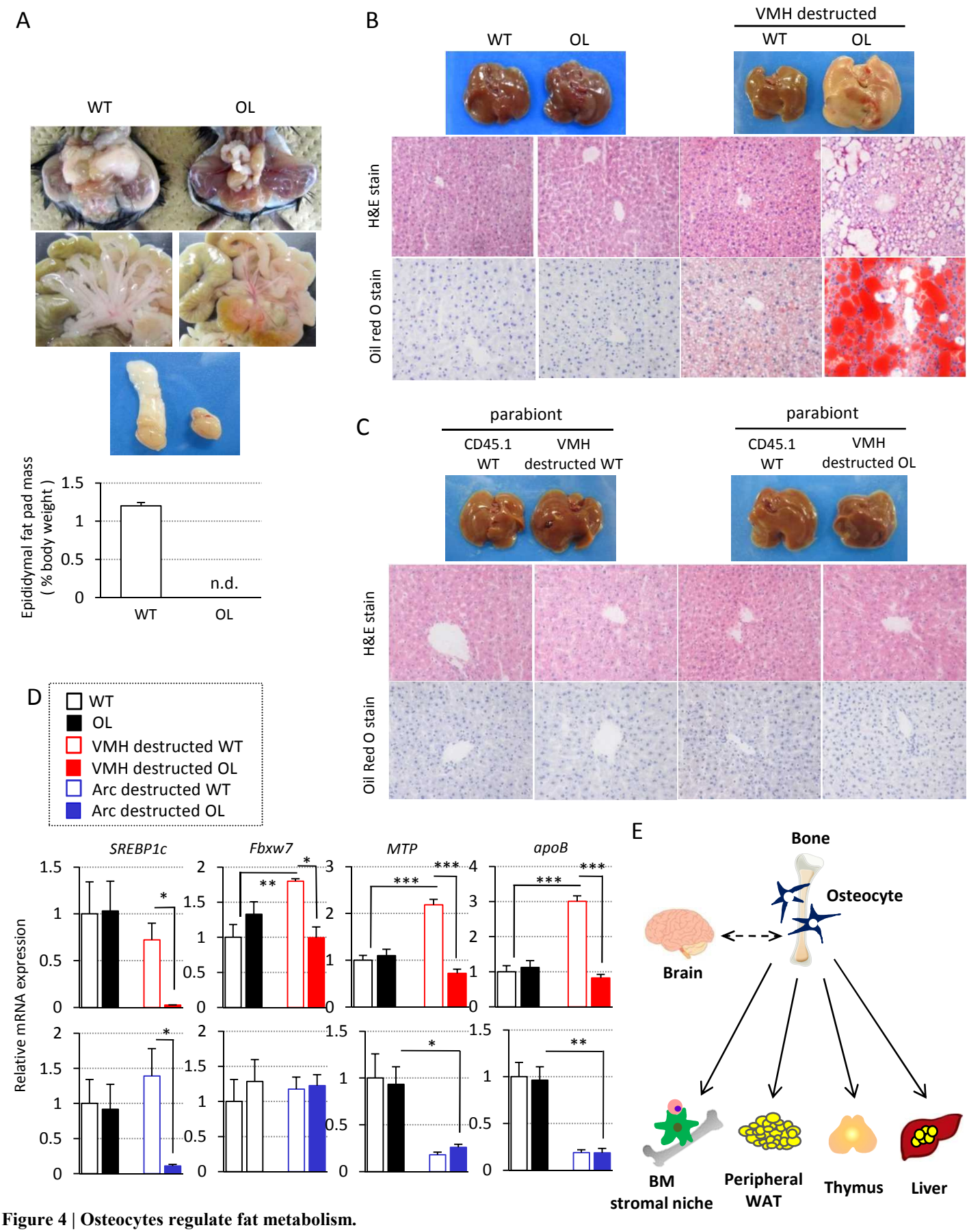

Figure 4 | Osteocytes regulate fat metabolism.

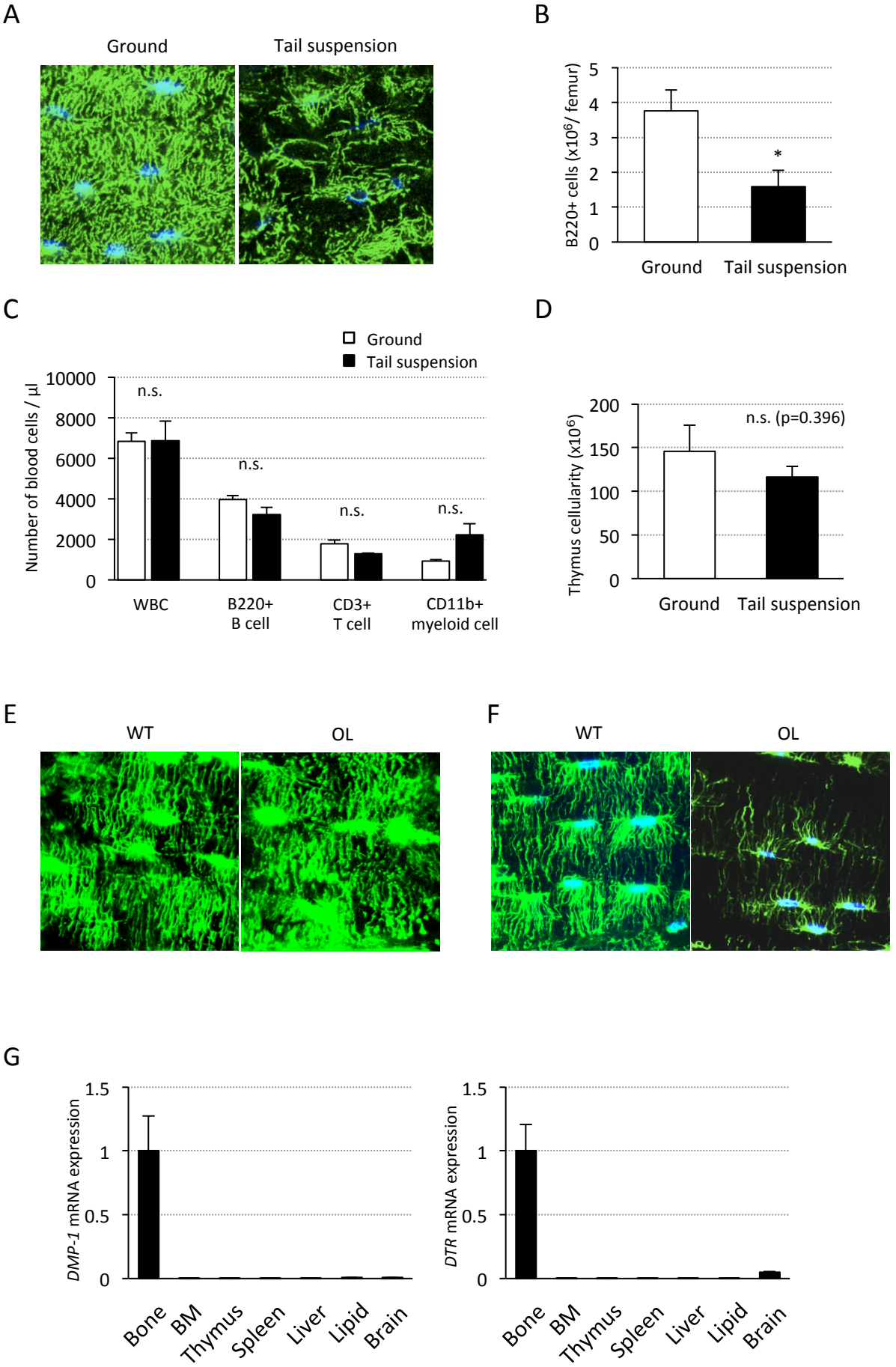

Supplemental Figure 1

Figure S1. Osteocyte-Network in Tail Suspension and OL Models, Related to Figure 1

The 8-week-old WT mice were subjected to skeletal unloading by tail suspension for 4 weeks. Mice on the ground served as controls. **A,** Immunofluorescence staining of unloading femoral cortical bone of ground and tail suspension mice. Images of CD44 staining were merged with DAPI. Tail-suspended mice showed disruption of osteocyte network formation as seen in OL mice. Original magnification, x100. **B,** BM nucleated cells from unloading femur were analyzed for surface expression of B cell marker B220 (n=3). **C,D,** Peripheral blood cells (C) and thymus cellularity (D) show no systemic alteration in lymphopoiesis in tail-suspended mice (n=3). **E,** Histological staining for visualization of bone interstitial fluid space using FITC. WT and OL mice showed similar interstitial space surrounding the osteocyte lacunae and canaliculae. Original magnification, X100. **F,** Alexa488-conjugated phalloidin, which binds specifically to actin filament, was used to stain the disruption of osteocyte network formation in OL mice. Original magnification, X100. **G,** Quantitative PCR analysis of *DMP-1* and *DTR* gene expression in indicated organs (n=5). All data were normalized to *β-actin*. Data are mean values ± SEM. *$p<0.05$.

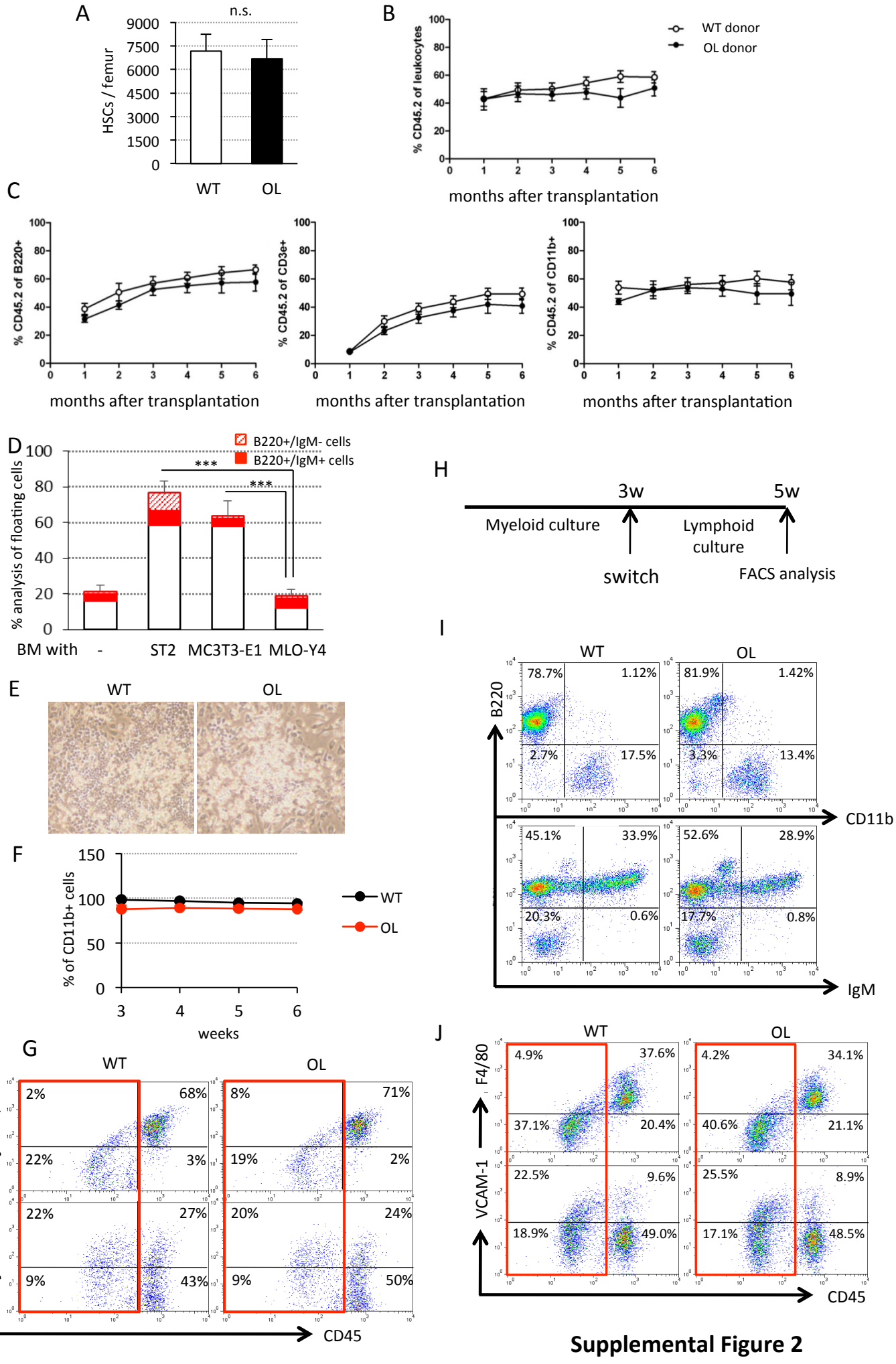

Supplemental Figure 2

Figure S2. Normal Stromal-Dependent Myelopoiesis in OL Mice, Related to Figure 2

A, Absolute cell number of HSCs (lineage-/IL-7Rα-/Sca-1+/c-kit+) in WT and OL mice BM (n=10). **B,C,** Competitive reconstitution was assessed by transplanting WT or OL mice bone marrow nucleated cells together with competitor CD45.1 cells into lethally-irradiated CD45.1 mice. Chimerism of total leukocytes (B) and lymphoid and myeloid cells (C) in peripheral blood was monitored monthly (n=7-8). Data are mean values ± SEM. **D,** Co-cultures of BM cells with osteolineage cell lines. Floating cells were analyzed for B220/IgM expression by FACS (n=7-8, ***p<0.001). The bars show the cells within the normal hematopoietic cell gate in Forward/Side scatter dot plot. Others and white bars may be dead cells and myeloid cells, respectively. Data are mean values ± SEM. **E,F,** M-LTBMC derived from WT (left panel) and OL (right panel) mice had similar appearance (E) and produced similar number of CD11b+ cells (F, n=4-5). **G,** FACS analysis of adherent cells in M-LTBMC. Similar numbers of stromal cells (red gated CD45- cells) were obtained (n=4-5). **H,I,J** Experimental design (H). M-LTBMC from WT and OL BM were initiated and maintained for 3 weeks, and then switched to B-LTBMC conditions. Two weeks after the switch, WT and

OL cultures produced similar numbers of B220+ cells, including those expressing surface IgM (I, n=3). **J,** FACS analysis of adherent cells in switch cultures. Similar numbers of stromal cells (red gated CD45- cells) were obtained (n=3).

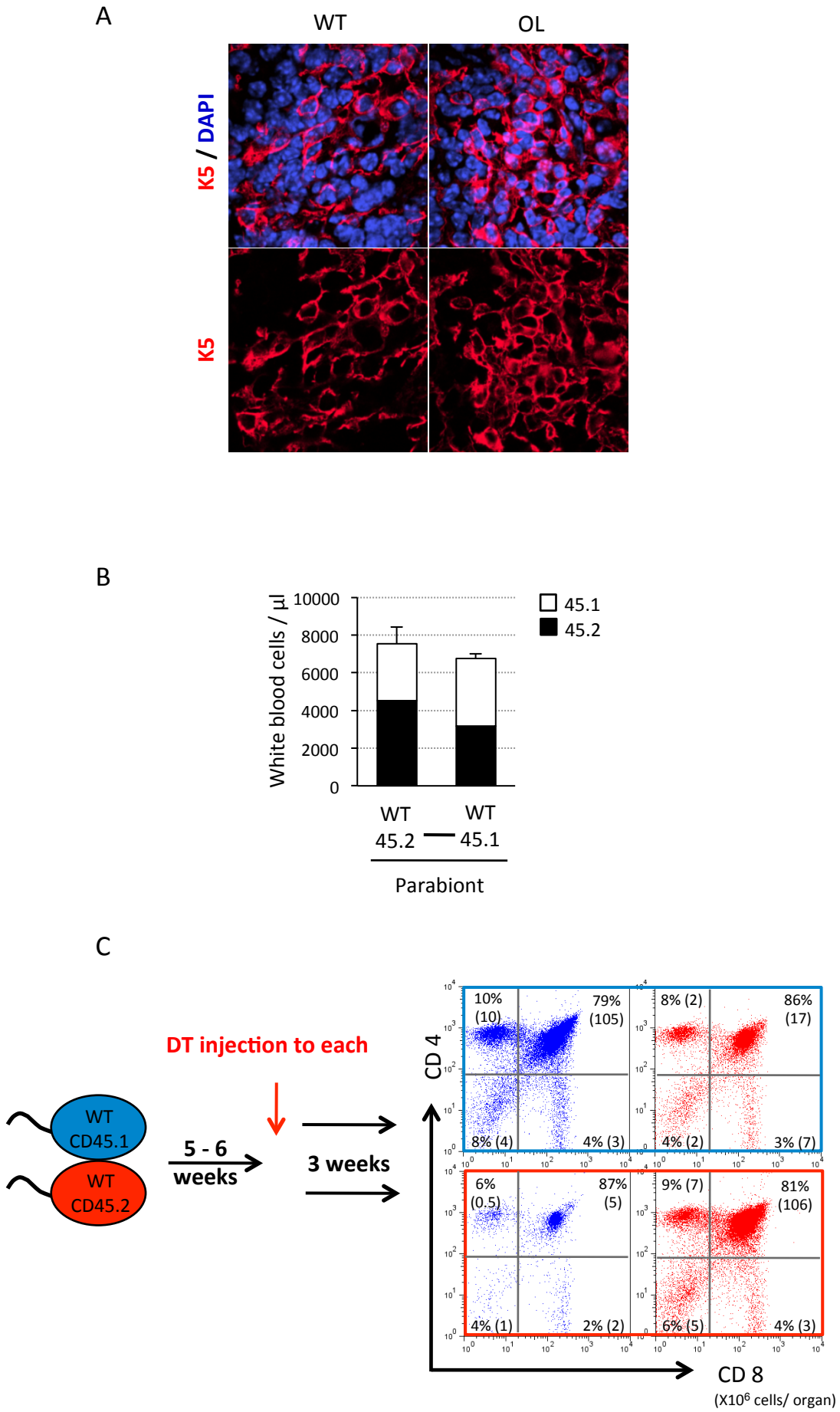

Supplemental Figure 3

Figure S3. Assessment of Thymic Microenvironment, Related to Figure 3

A, Immunofluorescent staining of K5 (red) and DAPI (blue) in WT and OL mice thymus. Magnifications x100. **B,** White blood cell (WBC) counts in peripheral blood of CD45.2 or CD45.1 mouse of a parabiotic pair 8 weeks after parabiosis. WBC that originated from CD45.1 (white area) and CD45.2 (black area) shared a common blood circulation (n=6). Data are mean values ± SEM. **C,** Experimental design. CD45.2 WT mouse was joined with CD45.1 WT mouse and maintained 5-6 weeks. Each mouse of a parabiotic pair was injected with DT and then after 3 weeks, thymic nucleated cells were isolated and analyzed for T cell markers by FACS (n=6).

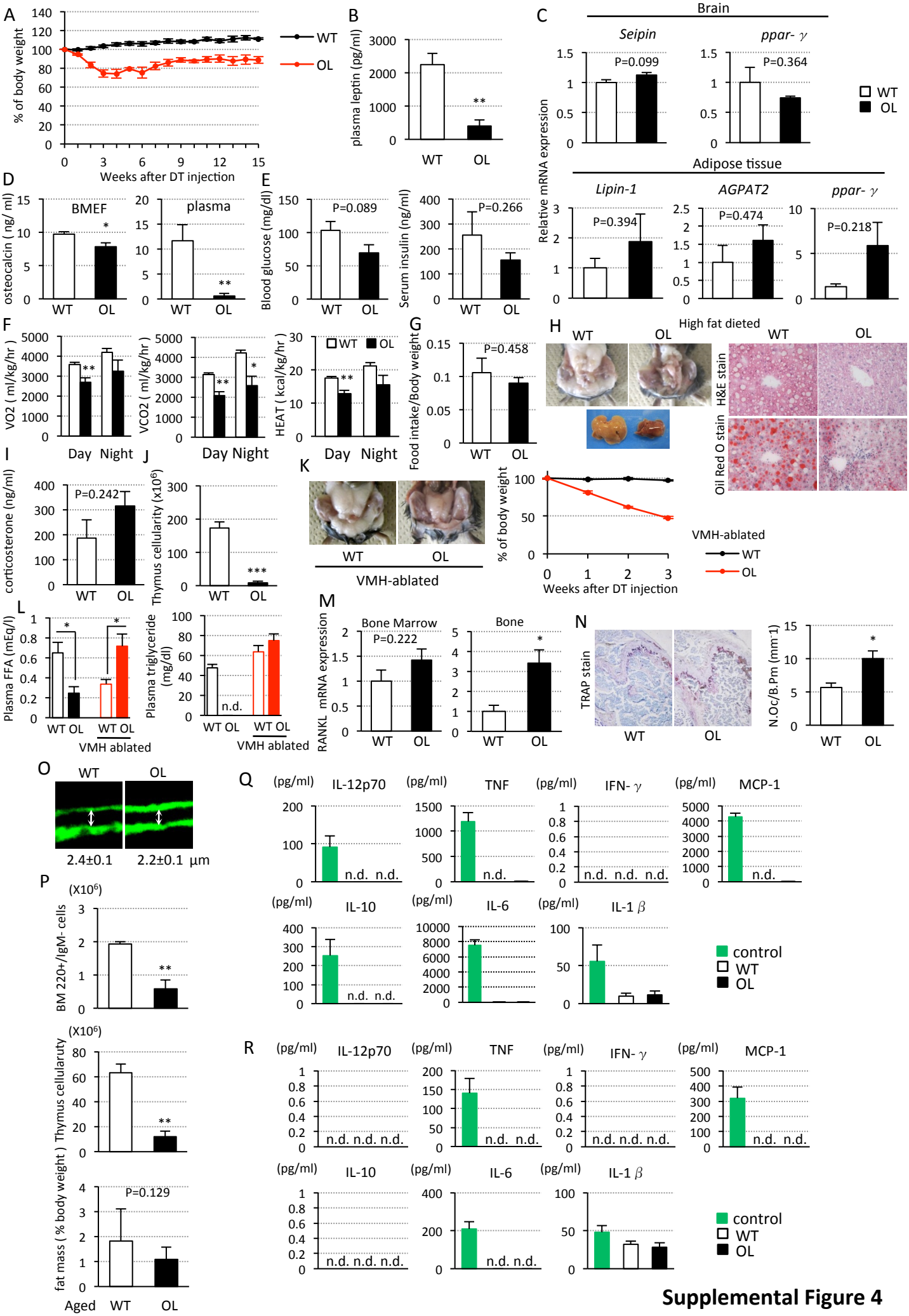

Supplemental Figure 4

Figure S4. Fat and Energy Metabolism in OL Mice, Related to Figure 4

A, The rate of body weights of WT or OL mice was measured at indicated time points after DT injection (n=3). **B,** Plasma leptin levels in WT and OL mice (n=3-5). **C,** Expression of lipodystrophy-related genes, including *seipin*, *lipin1*, and *AGPAT2*, and lipogenic gene, namely *ppar-*γ, in WT and OL mice brain or adipose tissue by real-time PCR (n=5). In this particular experiment, 15-week-old animals were injected with DT and then examined one week later in order not to lose all fat. **D,** Measurement of plasma and bone marrow extracellular fluid osteocalcin in WT and OL mice (n=5-7). **E,** Blood glucose and insulin concentrations from WT and OL mice, which were fasted for 12h. **F,** Energy-balance data at 2 weeks after DT injection: oxygen consumed (VO2), carbon dioxide produced (VCO2), and heat generated (n=4). **G,** Food intake was measured in WT or OL mice (n=4-6). Data shown were normalized by the body weight (food intake/body weight). **H,** Gross appearance of peripheral WAT and liver. After 11 weeks of high-fat diet starting at 4 weeks of age, WT and Tg mice were injected with DT. Hematoxylin and eosin (H&E)-stained and oil red O-stained sections of the liver are shown (original magnification x10). **I,** Plasma corticosterone levels in WT and OL mice (n=3). **J,** Thymus cellularity of

VMH-ablated WT or OL mice (n=3). **K,** Gross appearance of peripheral WAT and body weight change in VMH-ablated WT or OL mice (n=4-5). **L,** Concentrations of plasma free fatty acid (FFA) and triglyceride (n=4-5). Plasma samples were obtained from WT, OL, and VMH-ablated WT and OL mice, which were fasted for 12h. n.d.: not detected. **M,** RANKL mRNA expression in WT and OL mice (n=3-4). **N,** TRAP-stained sections of femoral metaphysis from WT and OL mice. Original magnification X4 (Left panel). Number of osteoclasts per bone perimeter (Right panel; N.Oc/B.Pm). **O,** Representative calcein-labeled sections of distal femur from WT (Left) and OL (Right) mice. **P,** Aged (48-54-week-old) WT and OL mice, models of slow bone remodeling, showed similar effects compared to 18-week-old OL mice (n=2-3). **Q,R,** Inflammatory cytokines in plasma (Q) and bone marrow extracellular fluid (R) in WT and OL mice. Samples from mice treated with lipopolysaccharide (50 μ g/mouse) were used as controls. n.d.: not detected. n=4-5. Data are mean values ± SEM. *p<0.05, **p<0.01, ***p<0.001.

Gene	Primer sequence
β-actin forward	5'-CTTCTTTGCAGCTCCTTCGTTG-3'
β-actin reverse	5'-CGACCAGCGCAGCGATATC-3'
DMP-1 forward	5'-GGCTGTCCTGTGCTCTCCCAG-3'
DMP-1 reverse	5'-GGTCACTATTTGCCTGTGCCTC-3'
DTR forward	5'-TCGAGAACTTCGCTGAGG-3'
DTR reverse	5'-CGCCAGTCACCAGTGCCGAG-3'
Srebp1c forward	5'-CATGGATTGCACATTTGAAG-3'
Srebp1c reverse	5'-CCTGTGTCCCCTGTCTCA-3'
Fbxw7 forward	5'-ACACGTTACAGGGACACACTAATAGAGT-3'
Fbxw7 reverse	5'-ACCACATGGATGCCATCAAAC-3'
MTP forward	5'-GTGGAGGAATCCTGATGGTGA-3'
MTP reverse	5'-TGATCTTAGGTGTACTTTTGCCC-3'
apoB forward	5'-CACGTGGGCTCCAGCATT-3'
apoB reverse	5'-TCACCAGTCATTTCTGCCTTTG-3'
Seipin forward	5'-GGCTCCTTCTACTACTCCCTACA-3'
Seipin reverse	5'-CCGATCACGTCCACTCTT-3'
Lipin1 forward	5'-TGG AAA TGC TCT GGC TGT GG-3'
Lipin1 reverse	5'-TGA AGA CTC GCT GTG AAT GG-3'
AGPAT2 forward	5'-TCT CTA CTG CGT GCT CTG CCT-3'
AGPAT2 reverse	5'-AGA GAT GAT GAC ACA GGG ACC-3'
ppar-γ forward	5'-TGACAGGAAAGACAACGGACAA-3'
ppar-γ reverse	5'-ATCTTCTCCCATCATTAAGGAATTCAT-3'
RANKL forward	5’-CCAGCCATTTGCACACCTCA-3’
RANKL reverse	5’-GTACCAAGAGGACAGAGTGACTTT-3’

Table S1. Primers used for PCR

The PCR protocol consisted of one cycle at 95°C (10 min) followed by 40 cycles of 95°C (30 s), 60°C (1 min), and 72°C (1 min).